ADVANCED MATERIALS
www.advmat.de

All-Oxide Metasurfaces Formed by Synchronized Local Ionic Gating

*Hyeon Han, Arpit Sharma, Jiho Yoon, Zhong Wang, Chris Körner, Hakan Deniz, Ankit K. Sharma, Fan Li, Chris Sturm, Georg Woltersdorf, and Stuart S. P. Parkin**

Ionic gating of oxide thin films has emerged as a novel way of manipulating the properties of thin films. Most studies are carried out on single devices with a three-terminal configuration, but, by exploring the electrokinetics during the ionic gating, such a configuration with initially insulating films leads to a highly non-uniform gating response of individual devices within large arrays of the devices. It is shown that such an issue can be circumvented by the formation of a uniform charge potential by the use of a thin conducting underlayer. This synchronized local ionic gating allows for the simultaneous manipulation of the electrical, magnetic, and/or optical properties of large arrays of devices. Designer metasurfaces formed in this way from $SrCoO_{2.5}$ thin films display an anomalous optical reflection of light that relies on the uniform and coherent response of all the devices. Beyond oxides, almost any material whose properties can be controlled by the addition or removal of ions via gating can form novel metasurfaces using this technique. These findings provide insights into the electrokinetics of ionic gating and a wide range of applications using synchronized local ionic gating.

1. Introduction

Ionic gating (IG) has attracted increased attention in recent years as a means of manipulating the physical properties of various thin films.[1–19] IG goes beyond conventional gating, such as that of a field effect transistor, by taking advantage of electrochemical changes engendered by large electric fields created within electric double layers (EDL) formed at an electrolyte/solid interface. Examples include thin films of an antiferromagnetic insulator, brownmillerite $SrCoO_{2.5}$, whose volume can be entirely converted into a ferromagnetic metal, the perovskite $SrCoO_{3-\delta}$ by IG[11,12] or vice-versa.[10,13]

To date, most studies of IG have been carried out using single devices with a three-terminal configuration.[1–19] The uniformity of the gating response across arrays of devices is critical for diverse applications. We show, by using time- and spatially-resolved in situ transport measurements and optical imaging, that the response to IG can be highly non-uniform when the film is initially insulating. Here we demonstrate that this limitation can be overcome by the formation of a uniform charge potential using a conducting thin underlayer. For large numbers of devices, this allows for what we will term "synchronized local IG". This concept enables us to locally manipulate the electric, magnetic, and optical properties of a given material so as to create arrays of distinct nano-sized regions within the host material over a large area. Thus, we can create all-oxide metasurfaces with properties beyond those of the individual nano-regions. As an example, we demonstrate the creation of designer planar oxide metasurfaces from continuous layers of $SrCoO_{2.5}$ that display an anomalous reflection of light at infrared wavelengths. Such metastructures in a single layer are distinct from conventional metasurfaces,[20–36] including those based on oxide materials,[31–36] which are typically composed of a dielectric oxide matrix decorated by deposited arrays of metallic structures. This new concept provides for the local control of electrical, magnetic, and optical properties over a large area and, thereby, the electrical creation of all-oxide metasurfaces.

2. Results and Discussion

We discuss IG on thin films of the brownmillerite $SrCoO_{2.5}$ (BM-SCO), which is an antiferromagnetic insulator that has oxygen vacancy channels (OVCs) within oxygen-deficient tetrahedrally coordinated cobalt layers (**Figure 1**a).[13] This phase is converted by IG to the perovskite $SrCoO_{3-\delta}$ (P-SCO) phase which is a

H. Han, A. Sharma, J. Yoon, Z. Wang, H. Deniz, A. K. Sharma, F. Li, S. S. P. Parkin
Nano Systems from Ions, Spins, and Electrons (NISE)
Max Planck Institute of Microstructure Physics
06120 Halle (Saale), Germany
E-mail: stuart.parkin@mpi-halle.mpg.de
C. Körner, G. Woltersdorf
Institute of Physics
Martin-Luther Universität Halle-Wittenberg
06120 Halle (Saale), Germany
C. Sturm
Felix Bloch Institute for Solid State Physics
Universität Leipzig
04103 Leipzig, Germany

The ORCID identification number(s) for the author(s) of this article can be found under https://doi.org/10.1002/adma.202401064

DOI: 10.1002/adma.202401064

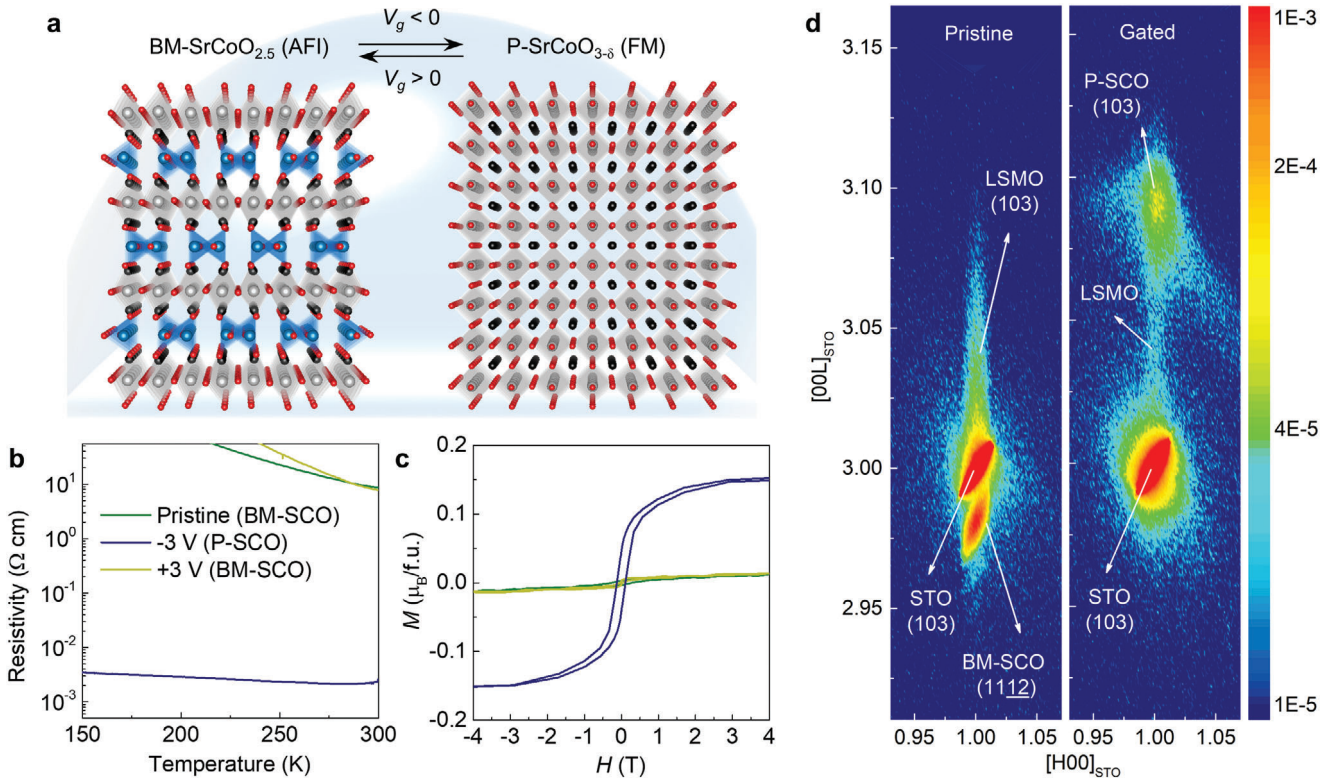

Figure 1. IG-induced phase transformation of $SrCoO_x$ films. a) Schematic illustration of IG-induced reversible phase transformation between BM- and P-SCO. The black, gray, blue, and red spheres indicate Sr, Co (octahedrally coordinated), Co (tetrahedrally coordinated), and O ions, respectively. b) Temperature-dependent resistivity of a 30 nm thick SCO thin film deposited on STO (001). The as-deposited BM-SCO is an insulator. After ionic liquid gating at −3 V for 10 min, the film is transformed to P-SCO with a decrease in resistivity by ≈3.5 orders of magnitude. P-SCO reverts to BM-SCO when a positive gate voltage of 3 V is applied for 10 min. c) Magnetic hysteresis loops measured at 100 K. A clear hysteresis loop is shown only for P-SCO. d) RSM of pristine and gated STO/LSMO/SCO. The formation of the P-SCO structure after gating is clear. All films and substrates exhibit identical (h00) values, indicating coherent epitaxial growth without any significant in-plane lattice relaxation.

ferromagnetic metal (FM). Epitaxial BM-SCO thin films, 30 nm thick, were deposited on $SrTiO_3$ (STO) (001) substrates using pulsed laser deposition (PLD). A metallic underlayer, formed from a 5 nm thick LSMO layer, was grown on the STO substrate prior to the growth of the BM-SCO layer. (Note that the transport and magnetic properties of the SCO_x films themselves were measured on films without the LSMO underlayer since the latter is both metallic and magnetic). These data show, consistent with prior studies,[10,13] that IG at negative gate voltages (V_g) results in a phase transformation from an insulating phase without any significant magnetization to an FM phase (Figure 1b,c; Figure S1a, Supporting Information). The reverse transformation takes place at positive V_g. The structures of both the pristine and gated SCO films were investigated by several techniques (Figure S1b–e, Supporting Information). Cross-sectional scanning transmission electron microscopy (STEM) using high-angle annular dark-field imaging shows that the as-deposited film has a BM structure with distinct OVCs that are oriented parallel to the substrate and that the gated structure has a typical cubic perovskite structure. The structures prepared with or without the LSMO underlayer are otherwise close to each other. The OVCs lead to distinct θ–2θ X-ray diffraction (XRD) peaks, for example, (002), (006), and (0010), due to the alternate stacking of layers of octahedrally and tetrahedrally coordinated Co. Reciprocal space mapping (RSM) studies (Figure 1d) reveal that all films and corresponding substrates exhibit nearly identical (h00) values, indicating coherent epitaxial growth without significant in-plane lattice relaxation, while the out-of-plane lattice parameters reveal an ≈3.3% contraction after gating.

Notably, the SCO films show distinct changes in their optical properties namely the refractive index (n) and extinction coefficient (k) after IG, indicating that this system can be used for optical devices, especially at infrared wavelengths (see Figure S2, Supporting Information).

To realize IG over large areas, an important question concerns the electrokinetics, that is, the time-dependent IG response across the film resulting from the electrically driven motion of ions. This is first investigated. Two counter electrodes (CEs) were deposited on both sides of the film. A gate electrode, formed from a thin Au foil with a large area comparable to that of the film, was placed close to the film (see **Figure 2**a,b; Figure S3a, Supporting Information). The film, gate electrode, and CEs were completely covered by the ionic liquid (IL). In addition, six channels, each 60 μm long and 20 μm wide, and spaced by 400 μm center to center, were patterned on the SCO films to measure the resistance (R) of each of the channels using current sources and nanovoltmeters, while applying V_g between the gate electrode and CEs using a source meter (See Experimental Section for more details).

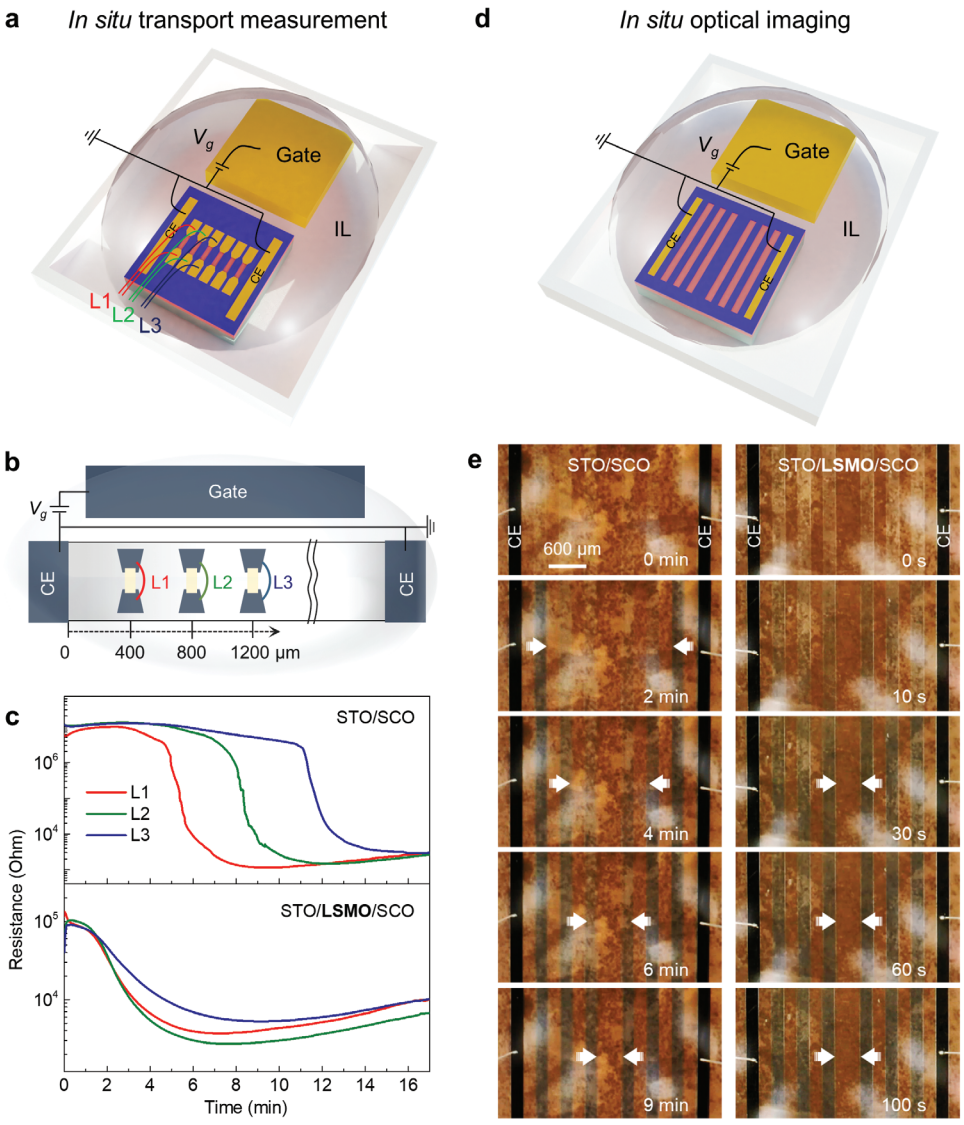

Figure 2. Time- and space-resolved in situ measurements during ionic gating. a,b) Schematics of the in situ transport measurement devices. The ionic liquid covers six electrically floating channels patterned in the device. CE is the counter electrode. The resistance of three channels was measured during IG. c) Time-dependent resistance (R) curves of three channels during gating for STO/SCO and STO/LSMO/SCO devices. d) Schematic of the in situ optical imaging device. The color change of the channels was recorded during IG. e) The recorded optical images versus gating time for STO/SCO (left) and STO/LSMO/SCO (right) devices. In the device without the LSMO layer, the channels clearly darken progressively from those closest to the CEs to those farthest away, while the device with conducting LSMO layer leads to a simultaneous gating over the entire area. The corresponding movies are shown in Videos S1 and S2.

Data for two sets of devices formed from SCO and LSMO/SCO films, respectively, are shown in Figure 2c. The SCO device shows a time-delayed response in the evolution of the resistance after the V_g is applied, which increases as the distance between the channel and the CE increases, whereas the time evolution of the resistance is the same for all channels for the LSMO/SCO device. Thus, these data indicate that the IG process is much more uniform for the wafer with the metallic underlayer.

The IG-induced material transformation was also monitored by changes in the optical properties of the individual channels. For this purpose, devices with six channels, each with an area of 800 × 200 μm^2, were fabricated, as shown in Figure 2d and Figure S3b (Supporting Information). For the wafer without the conducting underlayer, the channels are transformed progressively from those closest to the CEs to those farthest away, whereas, for the wafer with the metallic underlayer, all channels are transformed at similar rates (see Figure 2e, Video S1 for STO/SCO, and Video S2 for STO/LSMO/SCO, Supporting Information). Notably, these effects are even more critical when gating arrays of nano-sized regions (≈200 nm) in the form of V-shaped antennas (Figure S4, Supporting Information) to form optical metasurfaces. The fabrication process will be described, in detail, later. In Figure S5 (Supporting Information), the width of the antennas, after gating, becomes larger and merges

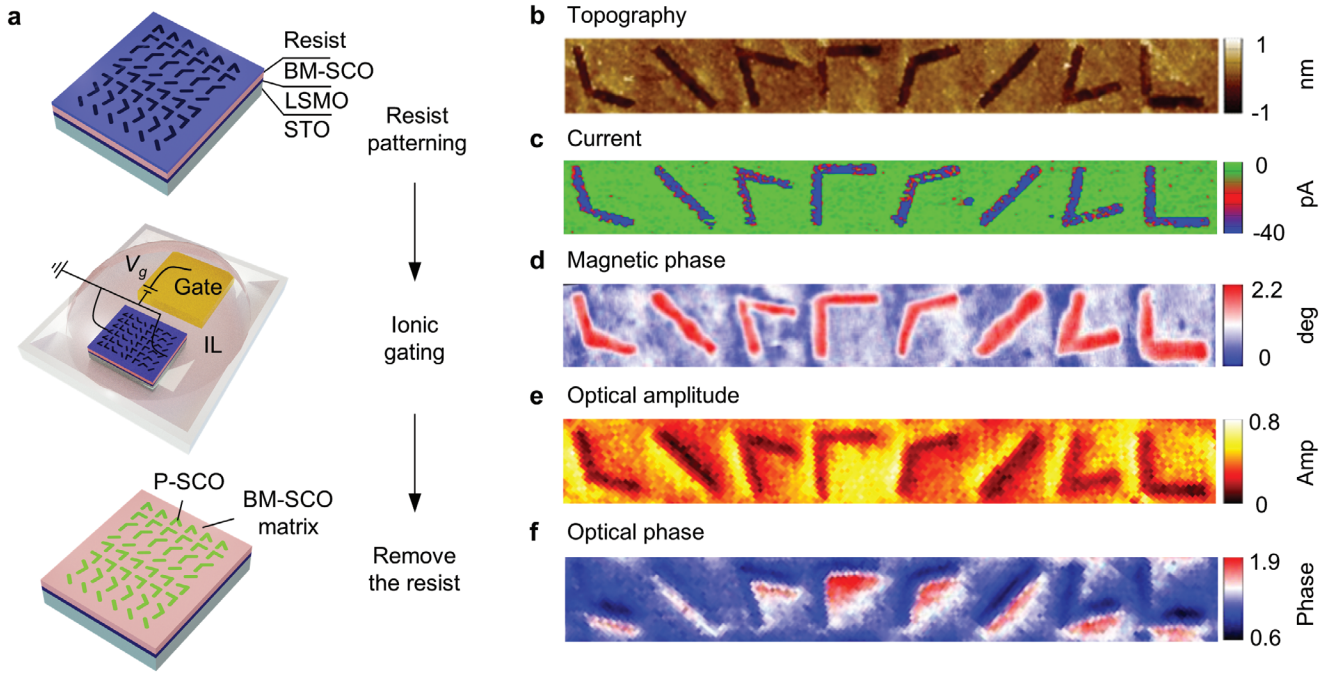

Figure 3. Emergent electric, magnetic, and optical textures by synchronized IG of $SrCoO_{2.5}$ thin films. a) Schematic diagram of the formation of an oxide metamaterial by synchronized local IG. b) Surface topography (AFM) and c) corresponding current map (CAFM) at room temperature. d) MFM phase image measured at 50 K and an in-plane magnetic field of 1 T. The gated structures (P-SCO) reveal larger current and higher phase shifts compared to the matrix area (BM-SCO), indicating the local creation of ferromagnetic metal textures within the antiferromagnetic insulating matrix. e) Amplitude and f) phase contrast of the optical near-field detected via s-SNOM using *x*-polarized incidence light. The low signals of the gated regions compared to the surrounding matrix and the observed phase shift of the scattered light are caused by the metallic absorption of the gated antennas.

together for the gated regions closer to the CE contacts for the wafer without the metallic underlayer. In contrast, the antennas for the LSMO/SCO device display a uniform size independent of their distance from the CEs. The optical reflection measurements (Figure S6, Supporting Information) carried out on these samples reveal clear anomalous reflections for the LSMO/SCO device, while the SCO device rather shows a noisy signal. Thus, understanding electrokinetics during IG is critical for both fundamental science and for applications.

The proposed mechanism of IG across the device is depicted in Figure S7 (Supporting Information). The ionic gating process is based on a two-step electrochemical reaction:[1,2,37] 1) a voltage (here the gate voltage, V_g) causes motion of ions within the ionic liquid and, thereby, the formation of an electric double layer in which, within the ionic liquid at the oxide layer surface, a layer of positively charged ions or negatively charged ions (i.e., the constituents of the ionic liquid), depending on the sign of the gate voltage, is formed. This leads to 2) screening by charge accumulation within the oxide layer and/or the subsequent ion migration into/out of the lattice. In our experiments, the intercalation of O^{2-} ions into the SCO film leads to a phase change from $SrCoO_{2.5}$ (BM-SCO) to $SrCoO_3$ (P-SCO). The observed non-uniform gating response is a consequence of the time delay in the formation of the EDL across the film surface. When we apply V_g to an insulating film, the charged ions of the IL initially accumulate near the CEs enabled by the capacitive coupling between the large area gate electrode and the two CEs. This leads to the formation of the EDL near these CEs on a part of the SCO layer in the vicinity of the CEs. This results in the metallization of the SCO via the addition of oxygen driven by the large vertical electric fields within the EDL. This leads to an increased capacitive coupling between the gate electrode and the device and, thereby, more oxygen is added to the SCO layer (within the channels) that are further removed from the CE. Thus, progressively, the channels in the SCO layer are metalized further and further away from the CE. Therefore, the process is limited by the gradual lateral metallization that starts from both of the CEs (which are positioned on either side of the SCO layer) toward the interior until all the SCO channels are metalized. When the metallic LSMO underlayer is used, then the entire SCO is capacitively coupled to the gate electrode from the beginning allowing for the simultaneous metallization of all the channels in the SCO layer at the same time. This is, as we find, a much faster process.

By using the concept of synchronized IG, we fabricated all-oxide metasurfaces, as illustrated in **Figure 3a**. Electron beam lithography (EBL) was used to pattern a resist layer that had been spin-coated onto the film. The subsequent development of the resist was used to create a mask with an array of nanoscopic orifices that allow for access to the surface of the film. We used the V-shaped antenna patterns that can effectively generate the anomalous reflection of light due to an abrupt phase shift in the light path.[22–25] The antennas consist of two arms that are connected to each other at specific angles (see Figure S4, Supporting Information). The individual V-antennas have a width (a) of ≈200 nm. Arrays of antennas are repeated with a period (Γ) of 16 µm. After the resist patterning, the two CE contacts were formed on the

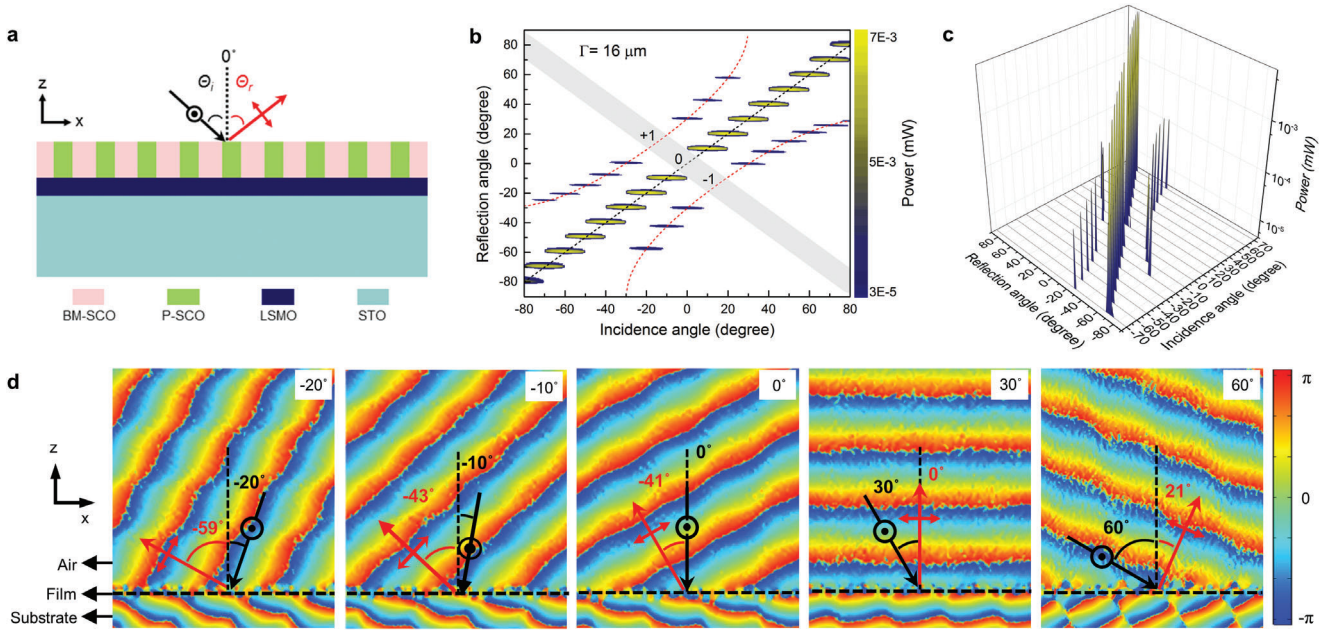

Figure 4. $SrCoO_x$ metasurface formed by synchronized local IG. a) Schematic view of the experimental setup for measurement of reflectivity from the meta-surface. The wavelength and incident power are 8.05 μm and 4 mW, respectively. The incident polarization is along the *y*-axis, while the reflection was measured along the *x*-polarization (cross polarization). b) Incidence angle-dependent reflection power maps. The black dashed line represents the ordinary reflection ($N = 0$), while the red dashed lines ($N = \pm 1$) are anomalous reflections calculated from the generalized Snell's law. The grey area indicates experimentally inaccessible angles. c) Incidence angle-dependent reflection power spectra. d) Finite element simulations of the $SrCoO_x$ metasurface at different incidence angles. The phase distribution of the reflected waves in the air is illustrated. The incident and reflection wave directions are indicated by the black and red arrows, respectively. The incident and reflection angles are shown in black and red text, respectively. The angles of the anomalous reflections are consistent with theoretical and experimental results.

device. An Au foil plate was placed next to the gate electrode in a boat. The device and gate electrode were then covered with a drop of ionic liquid. Then, V_g was applied between the gate electrode and CEs. The synchronized IG with the aid of the conducting LSMO layer allows for the local phase transformation of insulating BM-SCO into metallic P-SCO through these orifices. After gating, both the liquid and the resist mask were removed using chemical solvents (see Experimental Section for further details).

The V-antennas formed by synchronized local IG were examined by both atomic force microscopy (AFM) and conductive atomic force microscopy (CAFM) to investigate any changes in their size and edge quality as a function of gating time (Figure S8, Supporting Information). When the gating time is too long, the antennas start to become wider due to in-plane ionic diffusion. However, for optimized gating times (here 4 min for $V_g = -3$ V) well-defined antennas are formed, as shown by the AFM and CAFM maps in Figure 3b,c. Interestingly the antennas have a height that is ≈1 nm lower than the surrounding ungated regions, which is consistent with the contraction of the P-SCO lattice as compared to that of BM-SCO, as inferred from RSM. Note that the pristine film showed a smooth surface with a root-mean-square roughness of ≈0.37 nm (Figure S9, Supporting Information). Thus, such small changes (≈1 nm) in surface height after gating can be detected. The antennas show a significantly higher conductance than the surrounding matrix and, in addition, show a net magnetic moment, both properties expected for the FM P-SCO phase. The magnetism is readily seen using magnetic force microscopy (MFM) imaging (see Figure 3d).

To investigate the optical properties of the V-antenna arrays, scattering scanning near field optical microscopy (s-SNOM)[38] is utilized. This method allows for the detection of both the amplitude and phase of the scattered light, as shown in Figure 3e,f respectively. The amplitude map reveals an increased absorption in the gated regions. This is expected for the optical response of materials with a moderate imaginary part of the index of refraction (see Figure 1e,f). In the vicinity of the antennas, a phase shift of $\pi/2$ is observed and related to the metallic absorption.

Based on the significant change in reflectivity found in the SNOM measurements, we expect optical diffraction effects from the structured array in the far-field. A deviation from Snell's law induced by the periodically structured meta-surface is expected. The sub-wavelength pattern generates a spatially varying phase modulation which can be described by the generalized Snell's law of reflection:[24]

$$\sin\left(\theta_r\right) - \sin\left(\theta_i\right) = N\frac{\lambda_0}{2\pi n_i}\frac{d\Phi}{dx} \quad (1)$$

where θ_i is the incidence angle,θ_r is the reflection angle, λ_0 is the incidence wavelength, n_i is the refractive index of air (≈1), and $d\Phi/dx$ is the phase gradient along the film surface. N corresponds to the order of the diffraction, where $N = 0$ corresponds to ordinary reflection. In the far-field reflection measurements, *y*-polarized incident light illuminates the SCO metasurface formed by the synchronized local IG, as illustrated in **Figure 4a**. In Figure 4b, the *x*-polarized component of the reflected light is

mapped as a function of the angles of incidence and reflection. $N = \pm 1$ represents anomalous reflection, and the red dashed lines describe the calculated anomalous reflection angles based on the generalized Snell's law. The raw data of the reflection profiles are shown in Figure 4c and Figure S10 (Supporting Information). Then, the reflection efficiency (%) was calculated by dividing the reflection power (P_r) by the incidence power (P_i) of 4 mW, that is, the efficiency (%) = P_r/P_i (See Figure S11, Supporting Information). The efficiencies of the anomalous reflections (marked by asterisks) are as low as $\approx 10^{-2}$% which is due to the small optical contrast between the pristine and gated materials along with the signal degradation by the cross-polarization measurements.

To further support our experimental results, the propagation of the wavefronts emitted from the metasurface is simulated. Figure 4d illustrates the phase distribution of the reflected waves in air. The incident and reflection wave directions are indicated by the black and red arrows, respectively. The incident angle-dependent anomalous reflection angles are in good agreement with the generalized Snell's law and our experimental results (see Table S1, Supporting Information) as the anomalous reflection angles are mainly determined by the period (Γ) of the V-antenna arrays. These results demonstrate that the all-oxide nanostructure arrays created by the synchronized local IG function as an optical metasurface.

3. Conclusion

In summary, the electrical creation of all-oxide metamaterials composed of locally gated nano-structures was demonstrated via synchronized local IG of continuous oxide thin layers. We first investigated the kinetics of IG by in situ transport measurements and optical imaging, revealing that the typical three-terminal configuration[1–19] in combination with initially insulating oxide layers leads to highly spatially non-uniform gating. We show that this can be overcome by forming a uniform charge potential through a conducting (under) layer, enabling local control of electrical, magnetic, and optical properties over large areas in a $SrCoO_{2.5}$ thin film grown on a conducting LSMO layer. This concept was used to create all-oxide metasurfaces that exhibit anomalous optical reflection of light. This approach can be generalized beyond oxides, to a wide variety of other materials[8,9] whose physical properties are significantly modified by IG. Thus, diverse applications using our approach of synchronized local IG are possible.

4. Experimental Section

Film Growth: Epitaxial BM-SCO films were grown on STO (001) substrates by reflection high energy electron diffraction-assisted PLD using a 248 nm KrF excimer laser at a growth temperature of $T_g = 770$ °C. An oxygen partial pressure $p(O_2) = 10$ mT and a laser fluence of 0.8 J cm^{-2} were used. For a conducting underlayer, an LSMO film was grown at $T = 750$ °C, $p(O_2) = 200$ mT, using a laser fluence of 1 J cm^{-2} with post-annealing at $T = 750$ °C and $p(O_2) = 500$ Torr for 30 min. The thicknesses of SCO and LSMO layers were 30 and 5 nm, respectively.

Device Fabrication: All devices were fabricated using $\approx 5 \times 5$ mm^2 area chiplets cut from 1×1 cm^2 area substrates using a diamond scriber. V-antenna arrays were patterned onto the film using EBL (Figure 3a) with a positive-tone ≈200 nm thick resist (AR-P 6200.09). Gating of these devices was carried out by placing the fabricated devices inside a polytetrafluoroethylene (PTFE) boat and covering it and an adjacent gold plate (the gate electrode: 0.5 mm thick, and $\approx 5 \times 5$ mm^2 in area) with an ionic liquid that was dried in a vacuum chamber ($<10^{-6}$ mbar) at 110 °C for at least 12 h. DEME-TFSI (*N*, *N*-diethyl-*N*-methyl-*N*-(2-methoxyethyl) ammonium bis(trifluoromethanesulfonyl)imide) was used. After gating, the ionic liquid was first removed by acetone, and the resist was then removed using AR 300–76, and isopropyl alcohol, successively, at room temperature. The V-antenna design is shown In Figure S4 (Supporting Information).

Devices for in situ transport measurements and in situ optical imaging (Figure S3, Supporting Information) were fabricated by standard photolithographic techniques. Electrical contact pads were formed from an Au (70 nm) layer that was deposited on a Ru (5 nm) layer using ion beam sputtering (SCIA coat 200). Two CEs on either side of the chiplet and 6 pairs of electrodes for channel contacts were made. Then, windows in a photoresist layer were made for the six channels (60×20 μm^2 for in situ transport and 2800×200 μm^2 for in situ imaging) and CE contacts. Each CE was spaced 400 μm from the center of the closest channel, and the centers of each channel were spaced 400 μm from each other. Finally, the device was gated in a PTFE boat using the ionic liquid DEME-TFSI, whilst monitoring the resistance or color changes of each channel.

Characterization: $\theta - 2\theta$ XRD scans and RSM were carried out using a Bruker D8 Discovery X-ray four-circle diffractometer employing Cu-Kα radiation with a tube voltage of 40 kV and a current of 40 mA. Temperature and magnetic field-dependent magnetization measurements were carried out using an MPMS3 SQUID (Superconducting Quantum Interference Device) magnetometer. Surface topography and current maps were performed by conductive atomic force microscopy (Asylum Research) using Ti/Ir coated silicon tips. A 500 MOhm resistor was connected in series with the tip. MFM experiments were carried out in a variable temperature Attocube system equipped with a 2D vector superconducting magnet. Magnetic tips from Nanosensors (PPP-LM-MFMR) were used. STEM-HADDF measurements were carried out using a FEI Titan 80–300 transmission electron microscope at an acceleration voltage of 300 kV. The optical properties of the pristine and gated films were measured by an IRSE ellipsometer (J.A. Woollam). The data were analyzed by a two-layer model for the SCO film and STO substrate. The spectra were analyzed wavelength-by-wavelength, and then the analytic function was described by a dielectric function model. In situ transport measurements were carried out in a physical property measurement system (Quantum Design). Gate voltages were applied using a Keithley 2450A source meter. To measure the channel resistance, constant currents of 200 and 50 nA were applied to LSMO/SCO and SCO devices, respectively, using a Keithley 6221 current source, and the voltage was monitored by a Keithley 2182A nanovoltmeter. An optical microscope (Carl Zeiss, Axiotron 2) was used for the inspection of the fabricated devices. In situ optical microscopy imaging was carried out with a Dino-Lite digital microscope (5 MP, AnMo Electronics) using a white LED source. The films' resistivity measurements were carried out for a channel size of 65×30 μm^2 in a physical property measurement system (Quantum Design). Gate voltages were applied using a Keithley 2450A source meter. For the channel resistivity measurement, a constant current of 1 μA was applied using a Keithley 6221 current source, and the voltage was measured by a Keithley 2182A nano-voltmeter. s-SNOM (Neaspec) was used to characterize the optical response of the gated (−3 V, 10 min) STO/SCO device in the near field, with 5.1 μm light focused on the structures in a transmission geometry from the backside. This allowed for a homogeneous excitation with wavefronts parallel to the sample surface and, thus, an excitation phase independent of lateral position. The instrument used a Pt-coated cantilever operated in tapping mode ($f = 250$ kHz). The scattered light was collected by mirrors and focused on a mercury cadmium telluride detector. Angle-dependent optical reflection power was scanned. The incidence angle relative to the sample normal was varied from −80° to 80° by rotating the sample stage, while the detector was scanned from −90° to 90°. The incident wavelength and power were 8.05 μm and 4 mW, respectively. The incidence light was polarized along the *y*-axis, and a cross-analyzer in front of the detector was employed.

Finite Element Simulations: Finite element simulations of the electromagnetic field were made with Comsol Multiphysics 5.4. Far-field simulations were carried out for a physical volume of $32 \times 22 \times 89$ μm^3 using the wave optics module. An E_y-polarized electromagnetic wave (8 μm wavelength) was incident from the air side. A 1 μm-thick BM-SCO thin film with a 2×11-unit cell P-SCO antenna array on a 10 μm thick STO substrate was modeled. Here, the refractive index (n) and extinction coefficient (k) of BM-SCO and P-SCO (gated from BM-SCO) films that were measured using ellipsometry (Figure 1e,f) were used. Periodic boundary conditions were used for side boundaries to model an infinitely large meta-surface. Scattering boundary conditions were used for the top and bottom boundaries to absorb electromagnetic waves without any reflection. Tetrahedral meshes were used for all domains, and triangular meshes were used for all boundaries. The meshes at the thin film were no larger than 0.6 μm. The meshes in other regions were no larger than 1.6 μm.

Supporting Information

Supporting Information is available from the Wiley Online Library or from the author.

Acknowledgements

This project received funding from the European Union's Horizon 2020 research and innovation program under grant agreement No 737109. Funding was provided by the Alexander von Humboldt Foundation in the framework of the Alexander von Humboldt Professorship to S.S.P.P. endowed by the Federal Ministry of Education and Research. The authors thank Jae-Chun Jeon, Jaewoo Jeong, and See-Hun Yang for discussions. Z.W. thanks Yuechen Zhuang for guidance in carrying out the simulations.

Open access funding enabled and organized by Projekt DEAL.

Conflict of Interest

The authors declare no conflict of interest.

Data Availability Statement

The data that support the findings of this study are available from the corresponding author upon reasonable request.

Keywords

ionic gating, metasurfaces, synchronized local ionic gating, thin films

Received: January 21, 2024
Revised: April 20, 2024
Published online:

[1] J. Jeong, N. Aetukuri, T. Graf, T. D. Schladt, M. G. Samant, S. S. P. Parkin, *Science* **2013**, *339*, 1402.
[2] Y. Guan, H. Han, F. Li, G. Li, S. S. P. Parkin, *Annu. Rev. Mater. Res.* **2023**, *53*, 25.
[3] M. A. Hope, K. J. Griffith, B. Cui, F. Gao, S. E. Dutton, S. S. P. Parkin, C. P. Grey, *J. Am. Chem. Soc.* **2018**, *140*, 16685.
[4] Y. Chen, Z. Wang, S. Chen, H. Ren, B. Li, W. Yan, G. Zhang, J. Jiang, C. Zou, *Nano Energy* **2018**, *51*, 300.
[5] J. Jeong, N. B. Aetukuri, D. Passarello, S. D. Conradson, M. G. Samant, S. S. Parkin, *Proc. Natl. Acad. Sci. USA* **2015**, *112*, 1013.
[6] B. M. Lefler, W. M. Postiglione, C. Leighton, S. J. May, *Adv. Funct. Mater.* **2022**, *32*, 2208434.
[7] H. Han, Q. Jacquet, Z. Jiang, F. N. Sayed, J. C. Jeon, A. Sharma, A. M. Schankler, A. Kakekhani, H. L. Meyerheim, J. Park, S. Y. Nam, K. J. Griffith, L. Simonelli, A. M. Rappe, C. P. Grey, S. S. P. Parkin, *Nat. Mater.* **2023**, *22*, 1128.
[8] S. Z. Bisri, S. Shimizu, M. Nakano, Y. Iwasa, *Adv. Mater.* **2017**, *29*, 1607054.
[9] H. Du, X. Lin, Z. Xu, D. Chu, *J. Mater. Sci.* **2015**, *50*, 5641.
[10] N. Lu, P. Zhang, Q. Zhang, R. Qiao, Q. He, H. B. Li, Y. Wang, J. Guo, D. Zhang, Z. Duan, Z. Li, M. Wang, S. Yang, M. Yan, E. Arenholz, S. Zhou, W. Yang, L. Gu, C. W. Nan, J. Wu, Y. Tokura, P. Yu, *Nature* **2017**, *546*, 124.
[11] D. Zhang, H. Ishizuka, N. Lu, Y. Wang, N. Nagaosa, P. Yu, Q.-K. Xue, *Phys. Rev. B* **2018**, *97*, 184433.
[12] H. Han, H. Deniz, S. S. P. Parkin, *Proc. Natl. Acad. Sci. USA* **2023**, *120*, 2221651120.
[13] H. Han, A. Sharma, H. L. Meyerheim, J. Yoon, H. Deniz, K. R. Jeon, A. K. Sharma, K. Mohseni, C. Guillemard, M. Valvidares, P. Gargiani, S. S. P. Parkin, *ACS Nano* **2022**, *16*, 6206.
[14] S. G. Altendorf, J. Jeong, D. Passarello, N. B. Aetukuri, M. G. Samant, S. S. Parkin, *Adv. Mater.* **2016**, *28*, 5284.
[15] X. Leng, J. Pereiro, J. Strle, G. Dubuis, A. T. Bollinger, A. Gozar, J. Wu, N. Litombe, C. Panagopoulos, D. Pavuna, I. Božović, *npj Quantum Mater.* **2017**, *2*, 35.
[16] M. Wang, S. Shen, J. Ni, N. Lu, Z. Li, H.-B. Li, S. Yang, T. Chen, J. Guo, Y. Wang, H. Xiang, P. Yu, *Adv. Mater.* **2017**, *29*, 1703628.
[17] X. Yao, K. Klyukin, W. Lu, M. Onen, S. Ryu, D. Kim, N. Emond, I. Waluyo, A. Hunt, J. A. del Alamo, J. Li, B. Yildiz, *Nat. Commun.* **2020**, *11*, 3134.
[18] Q. Wan, M. Rasetto, M. T. Sharbati, J. R. Erickson, S. R. Velagala, M. T. Reilly, Y. Li, R. Benosman, F. Xiong, *Adv Intell Syst* **2021**, *3*, 2100021.
[19] J. Tang, D. Bishop, S. Kim, M. Copel, T. Gokmen, T. Todorov, S. Shin, K.-T. Lee, P. Solomon, K. Chan, W. Haensch, J. Rozen, in *IEEE Int. Electron Devices Meeting*, San Francisco, CA, USA, **2018**, pp. 13.1.1–13.1.4. https://doi.org/10.1109/IEDM.2018.8614551
[20] H.-T. Chen, A. J. Taylor, N. Yu, *Rep Prog Phys* **2016**, *79*, 076401.
[21] Q. He, S. Sun, S. Xiao, L. Zhou, *Adv. Opt. Mater.* **2018**, *6*, 1800415.
[22] N. Yu, F. Capasso, *Nat. Mater.* **2014**, *13*, 139.
[23] X. J. Ni, N. K. Emani, A. V. Kildishev, A. Boltasseva, V. M. Shalaev, *Science* **2012**, *335*, 427.
[24] N. F. Yu, P. Genevet, M. A. Kats, F. Aieta, J. P. Tetienne, F. Capasso, Z. Gaburro, *Science* **2011**, *334*, 333.
[25] B. J. Bohn, M. Schnell, M. A. Kats, F. Aieta, R. Hillenbrand, F. Capasso, *Nano Lett.* **2015**, *15*, 3851.
[26] N. I. Zheludev, Y. S. Kivshar, *Nat. Mater.* **2012**, *11*, 917.
[27] Y. Yang, I. I. Kravchenko, D. P. Briggs, J. Valentine, *Nat. Commun.* **2014**, *5*, 5753.
[28] H. S. Ee, R. Agarwal, *Nano Lett.* **2016**, *16*, 2818.
[29] Y. W. Huang, H. W. Lee, R. Sokhoyan, R. A. Pala, K. Thyagarajan, S. Han, D. P. Tsai, H. A. Atwater, *Nano Lett.* **2016**, *16*, 5319.
[30] Y. Wang, P. Landreman, D. Schoen, K. Okabe, A. Marshall, U. Celano, H. P. Wong, J. Park, M. L. Brongersma, *Nat. Nanotechnol.* **2021**, *16*, 667.
[31] Z. Li, Y. Zhou, H. Qi, Q. Pan, Z. Zhang, N. N. Shi, M. Lu, A. Stein, C. Y. Li, S. Ramanathan, N. Yu, *Adv. Mater.* **2016**, *28*, 9117.
[32] H. Kim, N. Charipar, E. Breckenfeld, A. Rosenberg, A. Piqué, *Thin Solid Films* **2015**, *596*, 45.
[33] T. Driscoll, S. Palit, M. M. Qazilbash, M. Brehm, F. Keilmann, B.-G. Chae, S.-J. Yun, H.-T. Kim, S. Y. Cho, N. M. Jokerst, D. R. Smith, D. N. Basov, *Appl. Phys. Lett.* **2008**, *93*, 024101.
[34] X. Duan, S. T. White, Y. Cui, F. Neubrech, Y. Gao, R. F. Haglund, N. Liu, *ACS Photonics* **2020**, *7*, 2958.
[35] M. J. Dicken, K. Aydin, I. M. Pryce, L. A. Sweatlock, E. M. Boyd, S. Walavalkar, J. Ma, H. A. Atwater, *Opt. Express* **2009**, *17*, 18330.

[36] M. D. Goldflam, M. K. Liu, B. C. Chapler, H. T. Stinson, A. J. Sternbach, A. S. McLeod, J. D. Zhang, K. Geng, M. Royal, B.-J. Kim, R. D. Averitt, N. M. Jokerst, D. R. Smith, H. T. Kim, D. N. Basov, *Appl. Phys. Lett.* **2014**, *105*, 041117.
[37] J. Luck, A. Latz, *Phys. Chem. Chem. Phys.* **2018**, *20*, 27804.
[38] T. Neuman, P. Alonso-González, A. Garcia-Etxarri, M. Schnell, R. Hillenbrand, J. Aizpurua, *Laser Photonics Rev.* **2015**, *9*, 637.